Correlation of spectral domain optical coherence tomography with histology and electron microscopy in the porcine retina

Wankun Xie[a,b], Min Zhao[a,b], Shu-Huai Tsai[a], William L. Burkes[a], Luke B. Potts[b], Wenjuan Xu[a], H. Ross Payne[c], Travis W. Hein[a,b], Lih Kuo[a,b], Robert H. Rosa Jr.[a,b,*]

[a] Department of Medical Physiology, Texas A&M University Health Science Center, Temple, TX, USA
[b] Department of Ophthalmology and Ophthalmic Vascular Research Program, Scott & White Eye Institute, Temple, TX, USA
[c] Image Analysis Laboratory, Texas A&M University College of Veterinary Medicine, College Station, TX, USA

ABSTRACT

Spectral domain optical coherence tomography (SD-OCT) is used as a non-invasive tool for retinal morphological assessment *in vivo*. Information on the correlation of SD-OCT with retinal histology in the porcine retina, a model resembling the human retina, is limited. Herein, we correlated the hypo- and hyper-reflective bands on SD-OCT with histology of the lamellar architecture and cellular constituents of the porcine retina. SD-OCT images were acquired with the Heidelberg Spectralis HRA + OCT. Histological analysis was performed using epoxy resin embedded tissue and transmission electron microscopy. Photomicrographs from the histologic sections were linearly scaled to correct for tissue shrinkage and correlated with SD-OCT images. SD-OCT images correlated well with histomorphometric data. A hyper-reflective band in the mid-to-outer inner nuclear layer correlated with the presence of abundant mitochondria in horizontal cell processes and adjacent bipolar cells. A concentration of cone nuclei corresponded to a relative hypo-reflective band in the outer portion of the outer nuclear layer. The presence of 3 hyper-reflective bands in the outer retina corresponded to: 1) the external limiting membrane; 2) the cone and rod ellipsoid zones; and 3) the interdigitation zone of photoreceptor outer segments/ retinal pigment epithelium (RPE) apical cell processes and the RPE. These correlative and normative SD-OCT data may be employed to characterize and assess the *in vivo* histologic changes in retinal vascular and degenerative diseases and the responses to novel therapeutic interventions in this large animal model.

1. Introduction

Spectral domain optical coherence tomography (SD-OCT) has proved to be a valuable approach to accurately measure retinal thickness and assess morphological changes *in vivo*, thus facilitating the longitudinal study of disease-related retinal alterations (Avery et al., 2015; Ribeiro et al., 2015). Numerous studies have employed the pig as a large animal model for the study of retinal diseases and therapeutic interventions, because the size, anatomy (including the dual vascular supply to the retina), vascular function, and immunology of the porcine eye are very comparable to the human eye (Adekunle et al., 2015; Bloodworth et al., 1965; Brant Fernandes et al., 2016; Fouquet et al., 2017; Hein et al., 2015; Koss et al., 2016; Mones et al., 2016; Rootman, 1971; Scott et al., 2014; Sorensen et al., 2012; Wang et al., 2014). In contrast to the human retina, the porcine retina does not have a fovea or macula; however, a "streak" of high cone density is located in a horizontal axis near the posterior pole of the porcine fundus, simulating

the human macula or area centralis (Hendrickson and Hicks, 2002). Although rod cells predominate over cones in both the porcine and human retina, the porcine retina contains less rods relative to cones compared to the human retina, with a rod to cone ratio of approximately 8:1 vs. 20:1, respectively (Curcio et al., 1990; Hendrickson and Hicks, 2002). The horizontal cells in the outer region of the inner nuclear layer (INL) in the porcine retina are much larger than in the human retina (Beauchemin, 1974). Although the thickness of the human retina has been studied extensively using multiple OCT instruments *in vivo* (Alamouti and Funk, 2003; Grover et al., 2010) and *ex vivo* (Yang and Du, 1999), limited information is available regarding the thickness of the porcine retina (De Schaepdrijver et al., 1990). In addition, retinal thickness varies depending upon the region measured (e.g., peripapillary, perifoveal, foveal, midperipheral, or equatorial) or at fixed distances from the optic nerve head (Carpenter et al., 2018). Because of the interspecies histologic variability, it may not be appropriate to simply apply human OCT interpretation to the porcine retina.

The pig model is being increasingly used to study retinal physiology and pathophysiology related to human diseases (Hein et al., 2012, 2015, 2016; Lim et al., 2018), and several investigators have used the porcine eye to study the application of intraoperative OCT for human vitreoretinal surgery (Asami et al., 2016; Ehlers et al., 2014; Hahn et al., 2013; Li et al., 2014). Recently, investigators have employed advanced clinical imaging techniques, including swept source and spectral domain OCT, and tissue-based biomarkers in the porcine eye in an attempt to reduce the utilization of nonhuman primates for toxicology studies (Atzpodien et al., 2016); however, the correlation between OCT images and the corresponding lamellar architecture and cellular constituents of the retina was not addressed or documented even though the anatomical attribution of OCT signals in the human retina have been studied extensively (Cuenca et al., 2018; Spaide and Curcio, 2011; Staurenghi et al., 2014). With advancement in OCT technology, the number and definition of the different bands on OCT images of the outer retina has been modified significantly in the last two decades (Jonnal et al., 2014; Spaide, 2012).

Other investigators have demonstrated that OCT-derived measurements are analogous to histologic analysis in various animal models, providing valuable information in the interpretation of OCT imaging (Dysli et al., 2015; Garcia Garrido et al., 2014; Gloesmann et al., 2003; Grieve et al., 2004; Knott et al., 2011). An "ultrahigh-resolution OCT" has been used previously to document different layers of the porcine retina (Gloesmann et al., 2003); however, the OCT correlation with retinal histology was limited by the OCT imaging techniques available at the time of publication (2003). With the rapid development of OCT technology in the last decade, the latest generations of commercially available SD-OCT with advances in resolution, scan density, speed, and signal-to-noise ratio allow for the discrimination of subtle alterations in the retinal layers. These newer generation OCT instruments are being widely used in both clinical and research laboratories (Fujimoto and Swanson, 2016). Although a more recent study correlated SD-OCT of the porcine optic nerve head with histological sections (Fatehee et al., 2011), information on the correlation between SD-OCT and histology, including electron microscopy, of the retina remains unavailable. Due to tissue shrinkage associated with tissue processing for histologic studies, it is difficult to directly correlate histologic sections of the retina with SD-OCT imaging. In the present study, we addressed this gap by comparing and correlating cross-sectional retinal SD-OCT images with histologic findings on light and electron microscopy in the porcine retina.

2. Materials and methods

2.1. Animals

All procedures were performed after approval by the Scott & White Institutional Animal Care and Use Committee with adherence to the National Institutes of Health Guide for the Care and Use of Laboratory Animals (8th Edition, 2011). Healthy male and female domestic pigs (Sus scrofa domesticus, Yorkshire; age range, 8–12 weeks; weight, 10–20 kg) were obtained from Real Farms (San Antonio, TX). All pigs were kept under a 12-h on/12-h off light/dark schedule with free access to food and water. A total of 9 pigs were examined.

2.2. SD-OCT image acquisition and analysis

The Heidelberg Spectralis HRA + OCT was used to document the microarchitecture of the retina. This device features a super luminescent diode at 870 nm as a low coherence light source. Scans were acquired at a speed of 40,000 A-scans per second and each two-dimensional B-scan contains up to 1536 A-scans. These images were taken with the equipment set at 30° field of view and with the software Heidelberg Eye Explorer (HEYEX version 6.6, Heidelberg, Germany).

The animals were sedated with 4–8 mg/kg Telazol intramuscularly and all experimental protocols were performed under isoflurane anesthesia (1.5–3.0%). Pupil dilation was achieved with 1% tropicamide eye drops (Bausch & Lomb Inc, Tampa, FL) before image acquisition. The animals were placed on a platform mounted in the chin rest of the imaging device with the eye in front of the system. A heat mat was used to keep the animal's normal core temperature at 39 °C during the acquisition process. Corneal hydration was maintained during retinal imaging through the administration of artificial tears (Refresh Optive®, Allergan Inc, Irvine, CA). A total of 14 eyes were scanned with SD-OCT imaging.

In order to create a reproducible reflectivity profile, the position of the retinal fundus image was standardized. The position of the eye was maintained with the optic disc exactly in the lower center of the fundus region visualized with the scanning-laser ophthalmoscopy (SLO) module of the Spectralis HRA + OCT (Xie et al., 2018 [Fig. 1]), and all OCT scans were acquired in this position. The retina was imaged by SD-OCT along the vertical meridian through the optic nerve head. Signal quality was greater than 25 db, scan speed was 40,000 A-scans per second, and 100 frames were averaged per B-scan to increase the signal-to-noise ratio. High-resolution mode was used with axial resolution at 3.9 μm and lateral resolution at 6 μm digital, using the enhanced depth imaging mode to optimize visualization of the choroid. Seven scans with an inter-scan distance at 240 μm were acquired. OCT scans were exported and converted into 8-bit grayscale images. Images were then processed with the ImageJ software package (Version 1.51j8; National Institutes of Health, Bethesda, MD), and reflectivity profiles were extracted from ten adjacent parallel lines which crossed perpendicularly to the OCT scan from the proximal (top) layer (the nerve fiber layer) to the distal (bottom) layer (the choroidal layer). For a visual representation of the underlying statistics of the data, reference lines indicating the 5, 50, and 95 quantiles were generated.

SD-OCT utilizes reflectance data from within the retina to generate an image of an *in vivo* section. This is accomplished by measuring reflectance at sequential depths in the retina with A- and B-scans. To obtain thickness measurements on the A-scans, layer lines automatically defined by Heidelberg software were manually adjusted. The distance between the internal limiting membrane (ILM) and retinal pigment epithelium (RPE) along the B-scan in SD-OCT images and the corresponding histologic sections were measured. SD-OCT measurements were assessed at 200 μm intervals along the vertical meridian from the optic nerve across the full length of the SD-OCT scan (8000 μm).

2.3. Tissue preparation for morphological analyses

Pigs were euthanized via exsanguination under isoflurane anesthesia after SD-OCT image acquisition. The eyes were enucleated and immediately placed in 4% paraformaldehyde (PFA). The anterior segment, lens, and vitreous were removed, leaving a posterior eyecup that contained the sclera, choroid, RPE, and neural retina. Every effort was made to avoid separation of the retina from the RPE during dissection and processing of the posterior eyecup. The posterior segment was then post-fixed by immersion in either 4% PFA for conventional histology and immunohistochemistry with paraffin-embedded or cryostat sectioning or 2% PFA/2% glutaraldehyde in phosphate-buffered saline (PBS) at 4 °C for 48 h for epoxy resin embedding and transmission electron microscopy.

2.4. Epoxy resin embedding and sectioning

Briefly, a 3 mm-wide strip of retinal tissue was dissected along the vertical meridian to include the optic nerve head and ora serrata. Following rinsing, secondary fixation in buffered 1% osmium tetroxide, final rinsing, and dehydration, tissue was embedded in Eponate 12 resin (Ted Pella, Redding, CA). Blocks of retinal tissue were cut into 500 nm-thick sections using the RMC PowerTome X Ultramicrotome (Boeckeler

Instruments, Tucson, AZ), stained with 1% toluidine blue (Sigma-Aldrich, St. Louis, MO), covered with a coverslip, and examined with light microscopy. Five eyes were processed for epoxy resin embedded light microscopy.

2.5. Immunofluorescence/immunohistochemistry

Immunofluorescence was performed using 4% PFA fixed tissue. After rinsing in increasing concentrations of sucrose diluted in PBS, the tissues were embedded and sectioned into 10 μm-thick sections with a cryostat and stored at −20 °C until further processing. Sections were treated with a primary monoclonal antibody to calbindin D-28K (Cat. #C 9848, Sigma, St. Louis, MO; 1:4000) to label horizontal cells. Slides were then washed and incubated in fluorescent conjugated secondary antibody (Alexa Fluor® 488 AffiniPure Donkey Anti-Mouse IgG, Cat. #715-545-150, Jackson Immuno Research Inc, West Grove, PA) in PBS. After preparation with fluorescent mounting medium, the slides were visualized and images were recorded with an inverted fluorescence microscope (Axiovert 200; Carl Zeiss MicroImaging, Thornwood, NY) as previously described (Hein et al., 2015). Three eyes were examined with immunofluorescence microscopy.

Immunohistochemistry was performed using the EnVision™ FLEX visualization system (Dako Inc., Carpinteria, CA). Briefly, tissue sections were deparaffinized, endogenous peroxidase activity was blocked, and high-temperature antigen retrieval was performed. Subsequently, sections were incubated in anti-calbindin D-28K antibody (Cat. #C 9848, Sigma, St. Louis, MO; 1:4000), followed by consecutive incubations with secondary antibody (EnVision™ FLEX/HRP Detection Reagent, Cat. # SM802, Dako Inc, Carpinteria, CA). Color development was achieved using the EnVision™ FLEX DAB + Chromogen and Substrate kit (Dako Inc., Carpinteria, CA). Hematoxylin was used for counterstaining of nuclei. Slides with stained tissue sections were then coverslipped and visualized with light microscopy (IX83; Olympus Corporation, Tokyo, Japan). Three eyes were studied with immunohistochemistry.

2.6. Transmission electron microscopy

The retinal tissue was prepared and processed for transmission electron microscopy (TEM) as previously described (Scott et al., 2011). Ultrathin (80 nm-thick) sections of the retina were examined with an FEI Morgagni 268 transmission electron microscope at an accelerating voltage of 80 kV. Digital images were acquired with a MegaViewIII camera operated with iTEM software (Olympus Soft Imaging Systems, Germany). TEM images were recorded at instrument magnifications of 1,800x to 44,000x. Three eyes were processed for TEM.

2.7. Data analysis

Sections matching the position of OCT scans were identified. Retinal blood vessels were used as landmarks for histomorphometric analysis of histologic sections and corresponding OCT images to account for tissue shrinkage. Image-analysis software (Photoshop CS; Adobe Systems, San Jose, CA) was used for linear scaling of photomicrographs to correct for volume changes of the tissue that occurred in the course of histologic processing, and the photomicrographs were overlaid on OCT images for correlation. Correlation between thickness measurements by OCT vs. histology was assessed by Pearson's correlation coefficient (GraphPad Prism, Version 6.01, GraphPad Software, La Jolla, CA). Differences in the retinal sub-layer thickness measurements in histologic sections and SD-OCT images were compared using Student's t-test (GraphPad Prism, Version 6.01, GraphPad Software, La Jolla, CA).
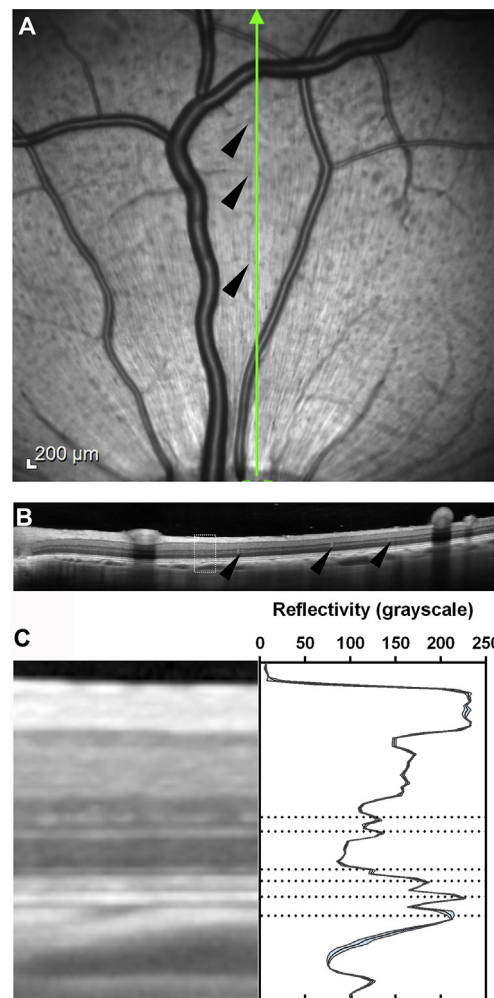
Fig. 1. SD-OCT Imaging of the Porcine Retina.
OCT vertical scan (A, B) through the superior optic nerve head and retina and schematic depiction (boxed area) of the 10 longitudinal adjacent pixel lines from which reflectivity profiles were extracted. Note the small retinal blood vessels (arrowheads) intersected by the green line/arrow indicating the scanned retina in the infrared image (A) and the corresponding hyper-reflectivity (arrowheads) on the OCT image (B). Higher magnification of the boxed area in the OCT image (C) shows the retinal layers (left panel) and correlation with the OCT reflectivity profile (right panel). Note the increased reflectivity of the nerve fiber and plexiform layers in the OCT scan (left panel) and the corresponding grayscale reflectivity (right panel). See Fig. 2 for OCT-histology correlation. (For interpretation of the references to color in this figure legend, the reader is referred to the Web version of this article.)

3. Results

3.1. OCT reflectivity profiles of the porcine retina

OCT imaging of the porcine retina was obtained (Fig. 1A and B), and OCT reflectivity profiles were generated from grayscale images with ImageJ software (Fig. 1C). As displayed in Fig. 1C, the retinal sublayers exhibited different reflective properties in SD-OCT imaging.

3.2. Correlation of SD-OCT, histology, and electron microscopy in the porcine retina

Histologic sections of the porcine retina were aligned with SD-OCT images acquired at the same location in the retina, with alignment of the corresponding ILM and RPE. As shown in Fig. 2A and B, the hyper- and hypo-reflective zones identified with the SD-OCT image
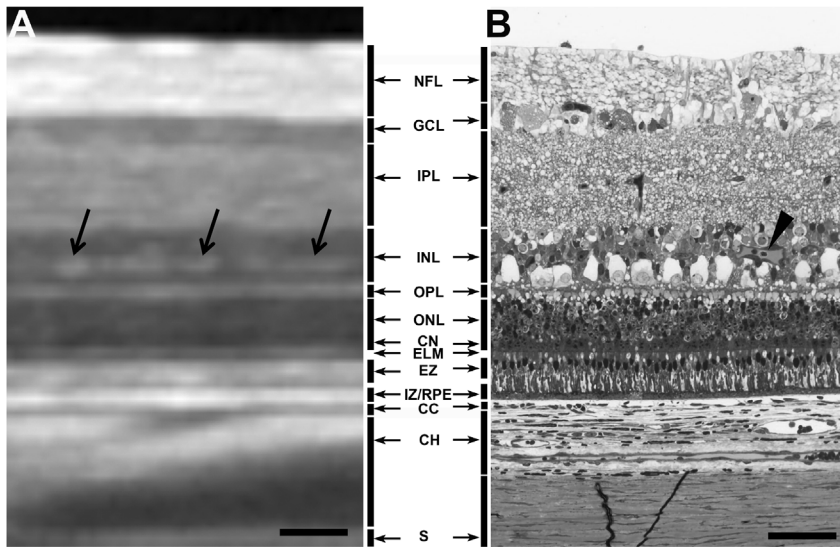
Fig. 2. Correlation of Retinal SD-OCT and Light Microscopy.

Cross-sectional OCT image of the porcine superior retina at 3000 μm from the superior margin of the optic nerve head in the vertical direction (A). Toluidine blue-stained epoxy resin embedded section (B) obtained from the corresponding retina. From the internal (top) to the external (bottom) retina, alternating light and dark bands of signal in the OCT image directly correlate with the retinal layers. Note that the discontinuous OCT hyper-reflective band (arrows) within the INL corresponds to the abundant cytoplasm of the horizontal cells on light microscopy and that the relative hypo-reflective band in the outer aspect of the ONL corresponds to the cone nuclei (CN). Note also longitudinal sectioning through a deep retinal capillary (arrowhead) in the INL. A thick hyper-reflective band (EZ) corresponds to the ellipsoid zones of the cones (more internal) and rods (more external) (see TEM, Fig. 6). Abbreviations: NFL, nerve fiber layer; GCL, ganglion cell layer; IPL, inner plexiform layer; INL, inner nuclear layer; OPL, outer plexiform layer; ONL, outer nuclear layer; CN, cone nuclei; ELM, external limiting membrane; EZ, ellipsoid zone; IZ/RPE, interdigitation zone/retinal pigment epithelium complex CC, choriocapillaris; CH, choroid; S, sclera. Scale bar: 50 microns.

corresponded with specific retinal layers. The ganglion cell layer (GCL) and outer nuclear layer (ONL) corresponded to hypo-reflective zones in SD-OCT. The nerve fiber layer (NFL), inner plexiform (IPL), outer plexiform layer (OPL), rod and cone ellipsoid zones (EZ), and interdigitation zone-RPE complex (IZ-RPE) complex corresponded to hyper-reflective zones in the SD-OCT images.

A "line" of cells was observed in the middle of the IPL (Fig. 2, see also Fig. 4A). A subtle decrease in the grayscale reflectivity is apparent in Fig. 1C corresponding to the same location. TEM revealed various cell types in the middle of the IPL, including endothelial cells (Xie et al., 2018 [Fig. 2A]), fibrous astrocytes (Xie et al., 2018 [Fig. 2B]), amacrine cells (Xie et al., 2018 [Fig. 3]), and Müller cells (Xie et al., 2018 [Fig. 3B]).

Histologic analysis of the INL revealed a row of large cells with abundant cytoplasm in the middle to outer portion of the INL (Fig. 2B, Xie et al., 2018 [Fig. 4]). Immunofluorescence (Fig. 3AA) and immunohistochemical (Fig. 3B) studies revealed that these large cells exhibited nuclear and cytoplasmic staining with anti-calbindin antibody (i.e., horizontal cells). On light microscopy, the horizontal cell cytoplasm appeared to correspond with a discontinuous hyper-reflective band within the hypo-reflective INL (Fig. 3). On electron microscopy, the horizontal cell processes in the middle to outer portion of the INL contained numerous mitochondria (Fig. 4 and Xie et al., 2018 [Fig. 5]). Adjacent bipolar cells also contained abundant mitochondria (Fig. 4 and Xie et al., 2018 [Fig. 5]). The nuclei of the horizontal cells resided in the outer portion of the INL (Fig. 2B and Xie et al., 2018 [Fig. 4]). The thickness of the hyper-reflective band in the INL as measured by SD-OCT was 18 μm, and the vertical thickness of the horizontal cell cytoplasm as measured by light micropcy was 20 ± 2 μm as shown in Table 1. The hyper-reflective band in the INL

appeared to correlate with the presence of numerous mitochondria in the cell processes of horizontal cells and the cytoplasm of adjacent bipolar cells (Figs. 2 and 4 and Xie et al., 2018 [Fig. 5]).

A distinct hypo-reflective zone in the outer portion of the ONL correlated with cone nuclei on histologic and TEM analyses (Figs. 1C, 2 and 5 and Xie et al., 2018 [Fig. 6]). The external limiting membrane (ELM) was a hyper-reflective band external to the ONL (Figs. 1C, 2, and 5). The hypo-reflective band external to the ELM corresponded to the myoid zone of the rod and cone inner segments (Figs. 2, 5 and 6). A hyper-reflective band measuring about 18 μm thick and located external to the myoid zone correlated with the cone and rod ellipsoid zones which contained a high concentration of mitochondria (Figs. 2 and 6 and Xie et al., 2018 [Fig. 4]). On TEM, the overlapping cone and rod ellipsoid zones measured about 18 μm in thickness (Table 1). A single hyper-reflective band measuring 15 μm thick corresponding with the photoreceptor outer segment-RPE IZ and RPE was identified external to a hypo-reflective band corresponding to the outer segments (Figs. 2 and 7 and Xie et al., 2018 [Fig. 6]). On TEM, the IZ-RPE complex measured 15 μm in thickness (Xie et al., 2018 [Fig. 6]). Abundant membranous organelles (i.e., endoplasmic reticulum and mitochondria) were observed in the RPE cytoplasm (Fig. 7). Long apical RPE cytoplasmic cell processes were intimately associated with the photoreceptor outer segments (Xie et al., 2018 [Fig. 6]). With enhanced depth imaging OCT, the choriocapillaris appeared as a distinct hypo-reflective layer external to the IZ-RPE complex (Figs. 1C and 2). Diffuse hyper-reflective signals interspersed with patches of hypo-reflective signals correlated with the pigmented choroidal stroma and the lumina of larger choroidal blood vessels, respectively (Fig. 2). Retinal blood vessels exhibited hyper-reflectivity on OCT imaging (Fig. 1 and Xie et al., 2018 [Fig. 7]).
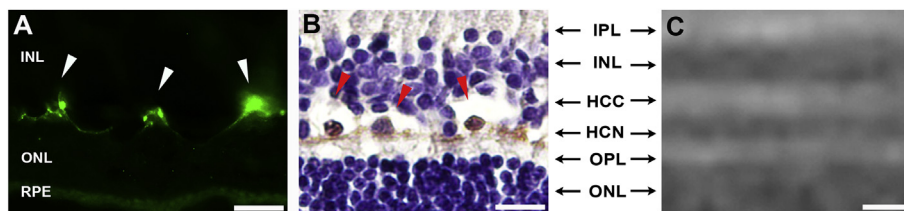
Fig. 3. Correlation of Histology and SD-OCT in the Inner Nuclear Layer of the Porcine Retina.

Immunodetection of calbindin D-28 (marker for horizontal cells) (arrowheads) in the porcine retina with immunofluorescence (A) and immunohistochemistry (B). Note the apical distribution of the cytoplasm in the horizontal cells (red arrowheads) and the nuclear and cytoplasmic staining of horizontal cells. Note that A is not in alignment with B and C due to differential tissue expansion and shrinkage with varying tissue processing methods (e.g., frozen sectioning in A and paraffin embedding in B). The hyper-reflective band in the INL correlates with the horizontal cell cytoplasm (C). Abbreviations: IPL, inner plexiform layer; INL, inner nuclear layer; HCC, horizontal cell cytoplasm; HCN, horizontal cell nucleus; OPL, outer plexiform layer; ONL, outer nuclear layer; RPE, retinal pigment epithelium. Scale bar: 20 microns. (For interpretation of the references to color in this figure legend, the reader is referred to the Web version of this article.)
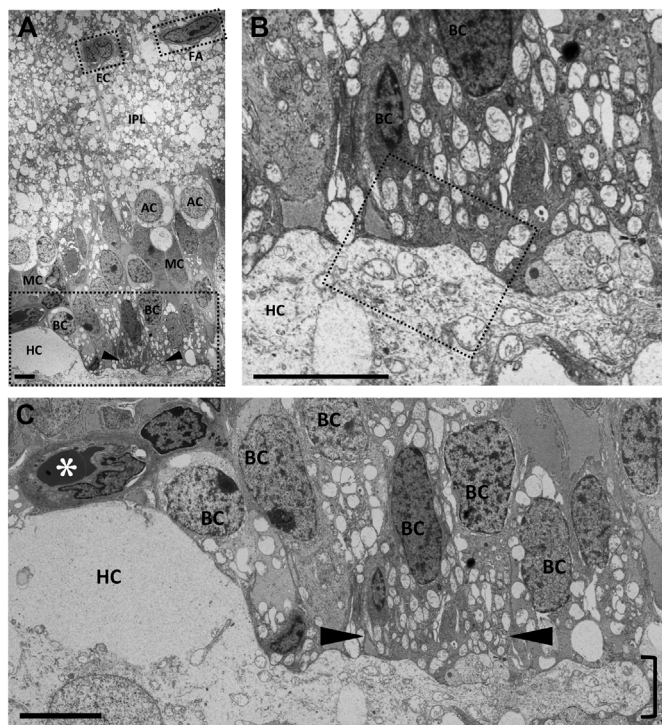
Fig. 4. TEM of the Inner Plexiform Layer (IPL) and Inner Nuclear Layer (INL) of the Porcine Retina.
Endothelial cells (EC) and fibrous astrocyte (FA) in the middle of the IPL (A, also see Xie et al., 2018 [Fig. 2]) for higher magnification electron micrographs) corresponded to discontinuous relative hypo-reflectivity in the IPL on SD-OCT. Various cell types are identifiable in the INL, including amacrine cells (AC), Müller cells (MC), bipolar cells (BC) and horizontal cells (HC). Numerous mitochondria are present in the bipolar cells (between arrowheads). Note the deep retinal capillary (asterisk) in the INL. The region between the arrowheads and in the boxed area in A is shown at higher magnification in B and C. Note the horizontal cell (HC) with a long cytoplasmic process (bracket) containing numerous mitochondria (B). Adjacent bipolar cells (BC) also contain abundant mitochondria (between arrowheads) (B). The boxed area in C is shown at high magnification in Xie et al. (2018) (Fig. 5). The presence of abundant mitochondria in this region of the INL correlates with a hyper-reflective band on SD-OCT. Scale bar: 5 microns.

Table 1
Comparison of retinal thickness measurements by SD-OCT imaging and histology.

Layer	SD-OCT (μm)	Histology (μm)	*P*-value
Total retinal thickness	290 ± 19	280 ± 14	0.37
Nerve fiber layer	66 ± 12	52 ± 9	0.04
Ganglion cell layer	18 ± 3	15 ± 3	0.12
Inner plexiform layer	68 ± 9	75 ± 10	0.24
Inner nuclear layer	41 ± 3	40 ± 3	0.57
Horizontal cell cytoplasm	18	20 ± 2	0.15
Outer plexiform layer	12 ± 2	13 ± 2	0.52
Outer nuclear layer	39 ± 6	40 ± 4	0.66
Ellipsoid zone	18	18	> 0.99
Interdigitation zone/RPE	15	15	> 0.99

The thickness of the retinal sublayers and total retina were measured by SD-OCT imaging and in corresponding histologic sections (3000 μm from the optic nerve head in the superior retina). Five eyes were examined and data are represented as Mean ± SD. The thickness of the horizontal cell cytoplasm, ellipsoid zone, and interdigitation zone/RPE were measured on transmission electron micrographs from 3 eyes. No significant differences in retinal thickness measurements were observed on OCT imaging vs. histologic sections, except for the nerve fiber layer.

In summary, in SD-OCT imaging of the porcine retina, the thick high-reflectivity grayscale band in the inner retina corresponded to the NFL and two thinner high-reflectivity grayscale bands in the outer retina (from internal to external) corresponded to the EZ and IZ-RPE. In the middle retina (from internal to external), the thick high-reflectivity grayscale band corresponded to the IPL and two thinner high-reflectivity grayscale bands corresponded to horizontal/bipolar cell cytoplasmic processes and OPL, respectively. The lowest reflective grayscale band in the retina corresponded to the ONL.

Retinal blood vessels were used as landmarks to assess tissue shrinkage associated with histologic processing, and tissue sections were compared to the OCT images in the transverse direction (Xie et al., 2018 [Fig. 7]). Compared to SD-OCT image measurements, the histologic sections demonstrated tissue shrinkage of 36 ± 4% in the transverse (i.e., horizontal) direction. SD-OCT and histomorphometric analysis were highly correlated with regard to total retinal thickness in the porcine retina (R^2 = 0.9886) (Fig. 8). The nerve fiber layer appeared significantly thicker in SD-OCT images compared to histologic sections; however, no significant volume changes in retinal thickness were observed in other sublayers of the retina (Table 1).

4. Discussion

The rapid development of OCT technology since its inception in 1991 has provided exquisite methods to identify and evaluate multiple layers of the eye wall and eye tissue, including the vitreoretinal interface, retina, RPE, Bruch membrane, and choroid (Huang et al., 1991). The pig is being employed increasingly as a large animal model for experimental and preclinical studies for human diseases, including retinal vascular (Hein et al., 2010, 2012, 2016) and degenerative diseases (Mones et al., 2016; Scott et al., 2014), and choroidal neovascularization (Tran et al., 2017). Despite the widespread adoption of SD-OCT instrumentation in research laboratories, histologic correlation of the porcine retina with SD-OCT data remains limited. Herein, we studied histology, immunostaining, electron microscopy, and the hypo- and hyper-reflective bands observed on SD-OCT in order to correlate these *in vitro* and *in vivo* assessments of the lamellar architecture and cellular constituents of the porcine retina.

We examined and compared histologic sections which matched the plane and retinal position of cross-sectional OCT scans. The OCT signals arise from different retinal sublayers with different optical properties (Huang et al., 1991). Differences in histologic architecture, including the number, distribution, metabolic activity, and type of cellular organelles, may lead to differences in the scatter and reflection of light (Tychinsky, 2009; Wilson et al., 2007). The subcellular components in addition to axodendritic layers may contribute to the varying reflective signals from different layers of the retina on high-resolution OCT (Anger et al., 2004). Controversy persists regarding the assignment of specific bands of OCT to specific retinal layers, since the reflective nature of a particular cell layer or subcellular component has not been definitively established. Furthermore, the anatomic components that give strong contrast in histologic staining may appear fairly inconspicuous in the tomogram (Gloesmann et al., 2003; Staurenghi et al., 2014). Layers rich in lipids may refract light and scale differently than tissue layers that have more aqueous components (Hoang et al., 2002). This might explain the observation that different sublayers may exhibit different scaling and measurements on SD-OCT imaging and histologic sections.

Our results demonstrated that the different layers of the porcine retina observed histologically corresponded with specific hyper- and hypo-reflective bands in SD-OCT images. Most layers of the porcine retina are quite similar to the human retina, corroborating the utilization of the pig as an excellent large animal model for the study of retinal diseases. Compared to the human retina, the major differences in the microscopic anatomy in the porcine retina include: 1) the lack of a fovea; 2) a higher density of cones through the visual streak across the
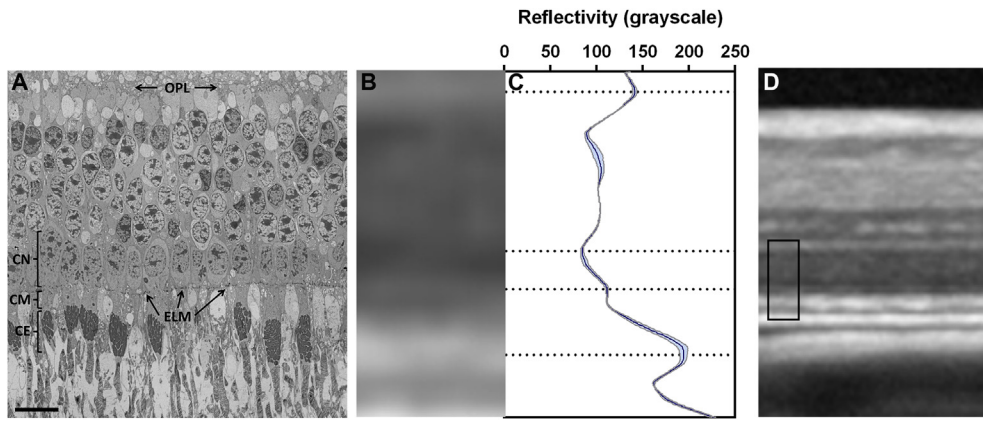
**Fig. 5. TEM of the Outer Nuclear Layer of the Porcine Retina.**
Note the concentration of cone nuclei (CN) in the outer aspect of the outer nuclear layer, immediately internal to the external limiting membrane (ELM) (A). This finding corresponded to a relative hypo-reflective layer in the outer portion of the ONL on SD-OCT imaging (B) as demonstrated in the reflectivity profile (C). The boxed area in the OCT image (D) is shown at higher magnification in B and correlated with the electron micrograph (A). Other abbreviations: outer plexiform layer, OPL; cone myoid, CM; cone ellipsoid, CE. Scale bar: 10 microns.

horizontal axis with prominent ellipsoidal mitochondria; 3) larger horizontal cells in the outer region of the INL; 4) a thicker IPL; and 5) a thinner OPL (Beauchemin, 1974; Curcio et al., 1990; Hendrickson and Hicks, 2002).

Interestingly, TEM revealed various cell types in the IPL: most commonly endothelial cells (Fig. 4A and Xie et al., 2018 [Fig. 2A]) and less frequently fibrous astrocytes (Xie et al., 2018 [Fig. 2B]), amacrine cells (Xie et al., 2018 [Fig. 3A]), and Müller cells (Xie et al., 2018 [Fig. 3B]). Ultrastructurally, the fibrous astrocytes were spindle-shaped with subplasmalemmal electron-dense microfilaments and patchy basement membrane, similar to fibrous astrocytes in the human retina (Rosa et al., 1996; Smiddy et al., 1989). The amacrine cells exhibited dispersed nucleoplasm, a distinct nucleolus, nuclear indentations, and electron-lucent cytoplasm (Xie et al., 2018 [Fig. 3A]). The Müller cells displayed comparatively more electron-dense nucleoplasm and

cytoplasm than the surrounding cells and extensive cellular processes wrapped around adjacent cell processes within the IPL (Xie et al., 2018 [Fig. 3B]). To the best of our knowledge, this is the first report of electron microscopic characterization of the discontinuous "line" of cells in the middle of the IPL in the porcine retina.

Our TEM data demonstrated that horizontal cells in the outer portion of the INL exhibited abundant cytoplasm, eccentric nuclei, and cytoplasmic processes containing numerous mitochondria (Fig. 4 and Xie et al., 2018 [Fig. 5]). Using immunohistochemical and immuno-fluorescent techniques, we demonstrated positive labeling of the horizontal cells with anti-calbindin antibody (Fig. 3A and B), which is consistent with previous studies showing calbindin-labeled horizontal cells in the pig (Atzpodien et al., 2016; Ghosh and Arner, 2010; Johansson et al., 2010). Our observations of the histologic and ultrastructural characteristics of the porcine horizontal cells are also
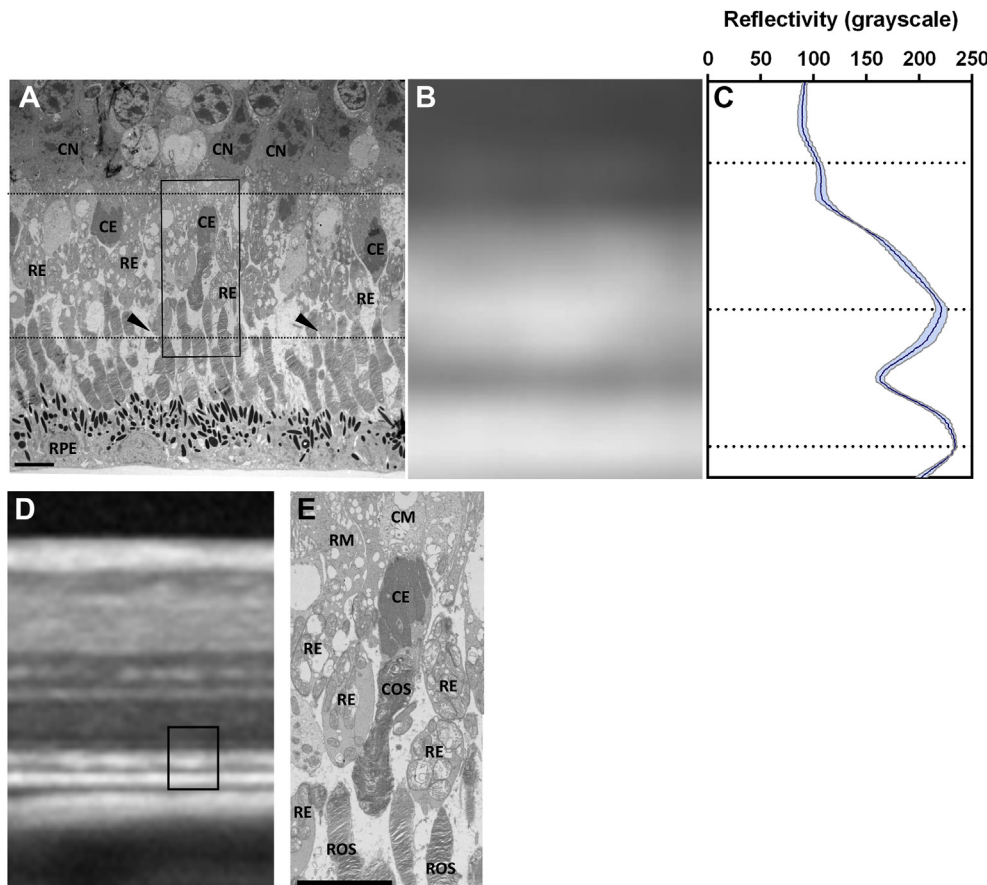
Fig. 6. TEM of the Photoreceptor Inner and Outer Segments.
The extent of the cone (CE) and rod (RE) ellipsoid zones with numerous mitochondria are demarcated by the dotted lines (A). The RE extend quite distally in the inner/outer segment region (arrowheads). This broad expanse of the CE and RE corresponds to the thickest of the 3 hyper-reflective bands in the outer retina on SD-OCT (B) as demonstrated in the reflectivity profile (C). The boxed area in the OCT image (D) is shown at higher magnification in B and correlated with the electron micrograph (A). Higher magnification (E) of the boxed area in A shows overlapping of the RE with the CE, cone outer segments (COS), and rod outer segments (ROS). Other abbreviations: CN, cone nuclei; RPE, retinal pigment epithelium; RM, rod myoid; CM, cone myoid. Scale bar: 5 microns.
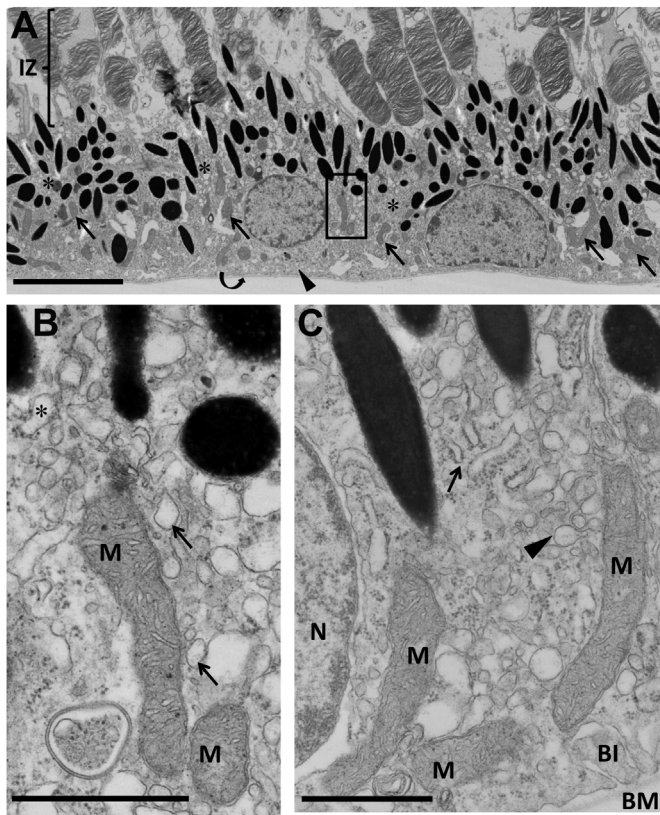
Fig. 7. TEM of the Retinal Pigment Epithelium (RPE) and the RPE-Photoreceptor Outer Segment Interdigitation Zone (IZ).
RPE apical cell processes and photoreceptor outer segments (A) are intimately associated in the interdigitation zone (IZ) (see also Xie et al., 2018 [Fig. 6]). The melanin pigment granules are concentrated in the apical RPE cytoplasm. Note the abundant endoplasmic reticulum (asterisks), mitochondria (arrows), and basal cytoplasmic membrane infoldings (arrowhead). These membranous profiles and the IZ appeared to correspond with the third hyper-reflective band on SD-OCT. The curved arrow indicates the RPE basement membrane. The boxed area is shown at higher magnification in B and shows extensive profiles of smooth (arrows) and rough (asterisk) endoplasmic reticulum and mitochondria (M). Note also the membrane-bound melanin pigment granules. A high magnification electron micrograph (C) of another RPE cell discloses several mitochondria (M), smooth (arrowhead) and rough (arrow) endoplasmic reticulum, and melanin pigment granules adjacent to the nucleus (N) in the basal cytoplasm. Note the basal cytoplasmic membrane infoldings (BI) and basement membrane (BM). Scale bars: A, 5 microns; B and C, 1 micron.

consistent with a previous ultrastructural study (Beauchemin, 1974). We found that bipolar and amacrine cell nuclei were localized to the inner to middle regions of the INL and exhibited a smaller cell size (Figs. 2B, 4A and 4B) compared to the horizontal cells. Poor lateral resolution of the SD-OCT images and smearing in the transverse direction might contribute to the discontinuous hyper-reflective band in

the INL in addition to the lateral spacing of the horizontal cells in the INL (Figs. 1C and 2). Previous OCT studies of the porcine retina have not reported the additional hyper-reflective band in the INL, perhaps because a different OCT instrument was utilized (Gloesmann et al., 2003; Grieve et al., 2004), or only the optic nerve head was scanned (Fatehee et al., 2011). However, in a previous study of the porcine retina (Gloesmann et al., 2003), a subtle hyper-reflective band is present in the middle of the INL (in their Fig. 1), which may correspond to the hyper-reflective band that we have identified and correlated with a high concentration of mitochondria in the horizontal and bipolar cells as described above. In other species including in mice, rats, gerbils, dogs, cats, and cynomolgus monkeys, no additional hyper-reflective band has been described in the INL (Berger et al., 2014; Dysli et al., 2015; Garcia Garrido et al., 2014; McLellan and Rasmussen, 2012). The presence of a hyper-reflective band on SD-OCT in the INL of the porcine retina differs from the INL of the human retina, which is represented by a more homogeneous hypo-reflective band on SD-OCT.

The OPL of the porcine retina was identified in SD-OCT imaging as a narrow hyper-reflective band external to the INL and corresponded to a thin layer of apparent cytoplasmic processes histologically (Figs. 1C, 2 and 5 and Xie et al., 2018 [Fig. 4]). In the OPL, the synapses between cone pedicles and rod spherules with dendrites of horizontal and bipolar cells may give rise to high scattering of light (Beauchemin, 1974; Staurenghi et al., 2014) and contribute to the hyper-reflective band on OCT (Fig. 5 and Xie et al., 2018 [Fig. 4]). External to the OPL, the ONL appeared as a thick hypo-reflective band on SD-OCT and corresponded to the multilayered cell bodies (nuclei) of rods and cones observed histologically (Figs. 1C, 2 and 5 and Xie et al., 2018 [Figs. 4 and 6]). In contrast to the human retina, the cone nuclei in the porcine retina are situated in the outer or external aspect of the ONL (Beauchemin, 1974). Interestingly, the localization of these cone nuclei correlated with a relative hypo-reflective zone in the outer portion of the ONL (Figs. 1C, 2 and 5 and Xie et al., 2018 [Figs. 4 and 6]).

In contrast to the 4 outer retinal hyper-reflective bands described with SD-OCT imaging of the human retina (Ross et al., 2015; Spaide, 2012; Spaide and Curcio, 2011; Staurenghi et al., 2014), we observed 3 outer retinal hyper-reflective bands in the porcine retina (Figs. 1C and 2). The first hyper-reflective band in the outer retina corresponded to the ELM (Figs. 2 and 5). The ELM is difficult to measure in histologic sections and appears thicker in SD-OCT imaging. The second hyper-reflective band corresponded to the ellipsoid zones of the cone and rod inner segments, which contain abundant mitochondria (Figs. 2 and 6). Interestingly, in the porcine retina, the rod ellipsoid zones overlap the cone ellipsoid zones, the cone outer segments, and the proximal rod outer segments (Fig. 6). On TEM, the cone-rod ellipsoid zones measured 18 μm in total thickness (Fig. 6A). The extensive area occupied by the cone and rod ellipsoid zones with a high concentration of mitochondria in this region generated the thickest of the 3 outer retinal hyper-reflective bands, measuring about 18 μm thick on SD-OCT imaging (Fig. 2). The presence of abundant mitochondria in the ellipsoid zone of the inner segments (Cuenca et al., 2018; Lu et al., 2012) and translocation of mitochondria toward cone nuclei in outer retinal tubulation
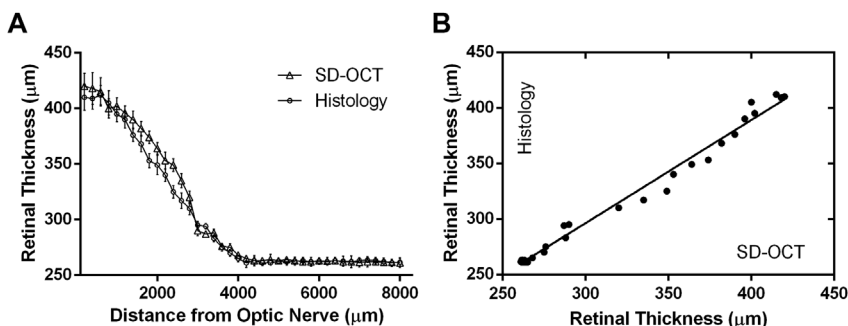
Fig. 8. Correlation of Porcine Retinal Thickness Measured by SD-OCT and Histology.
Porcine retinal thickness was measured at 200 μm intervals along the vertical meridian from the optic nerve head in histologic sections and across the full length of SD-OCT scans (8000 μm). Scatter plot of retinal thickness (A) along the vertical meridian of the superior retina measured from the optic nerve head to the midperipheral retina by SD-OCT and histology, and the regression plot (B) revealed significant correlation ($R^2 = 0.9886$) of retinal thickness measurements by SD-OCT and histology. Vertical bars represent ± SEM.

(Litts et al., 2015a,b, 2018; Schaal et al., 2015) have been correlated previously with hyper-reflectivity on OCT imaging. The third and most reflective band in the outer porcine retina on SD-OCT imaging measured about 15 μm thick and correlated with the 1) the interdigitation zone (IZ) between the RPE apical cell processes and photoreceptor outer segments and 2) the RPE (Figs. 1B and 2). On TEM, the IZ-RPE layer measured about 15 μm thick (Xie et al., 2018 [Fig. 6]). Similar to human eyes, the melanin pigment granules were concentrated in the apical cytoplasm of the RPE in the porcine retina; however, pigment granules were also observed in the basal and mid-cytoplasm (Fig. 7). RPE mitochondria were most abundant in the basal to mid-cytoplasm in the porcine retina; however, mitochondria were also observed in the apical cytoplasm (Fig. 7). Abundant smooth endoplasmic reticulum was present throughout the RPE cytoplasm (Fig. 7). We propose that the third hyper-reflective band in the porcine retina was generated by the extensive membranous profiles associated with the overlapping RPE apical cell processes and photoreceptor outer segments, abundant endoplasmic reticulum and mitochondria in the RPE cytoplasm, and extensive RPE basal cytoplasmic infoldings (Fig. 7 and Xie et al., 2018 [Fig. 6]).

Recently, the third and fourth outer retinal hyper-reflective bands in OCT imaging of the human macula were attributed to phagosomes in the apical cytoplasm of the RPE and abundant mitochondria in the basal cytoplasm of the RPE, respectively (Cuenca et al., 2018). In addition, a concentration of melanosomes in the mid-cytoplasm of the RPE was proposed to cause the hypo-reflective band interposed between the third and fourth outer retinal hyper-reflective bands (Cuenca et al., 2018). The average height of the RPE in the posterior pole was previously reported to be 9–14 μm in the literature (Hogan et al., 1971; Kaczurowski, 1962; Ts'o and Friedman, 1967, 1968). Interestingly, we found that the maximal height of the RPE (not including the apical cell processes in the interdigitation zone) was about 10 μm in the porcine retina (Fig. 5A). Differences in tissue fixation and processing might account for differences in RPE cell height measurements; however, multiple independent studies of human eye tissue have generated similar results as noted above. The average height (or vertical dimension) of RPE cell nuclei in the posterior pole of the human eye was reported to be 3–4 μm (Kaczurowski, 1962), and the average diameter of human RPE cell nuclei in the posterior pole (without reference to vertical vs. horizontal axes of measurement) was 5–12 μm (Ts'o and Friedman, 1967). The lack of a fourth hyper-reflective band in the porcine outer retina might be attributed to more random distribution of the RPE nuclei within the cytoplasm (Fig. 7 and Xie et al., 2018 [Figs. 4 and 6]) compared to the human outer retina. Although the specific anatomic correlation of these hyper-reflective outer bands is still controversial in the human retina, we observed similar hyper-reflective outer bands in the porcine retina with SD-OCT imaging and histologic and ultrastructural correlation.

In this study, we used epoxy resin embedded tissues and sectioning for conventional histology to minimize tissue shrinking. The measurement of retinal thickness by histology and SD-OCT imaging disclosed high-level correlation between the two forms of analysis of neural retinal thickness in the porcine retina (Fig. 8). The correlation between histology and OCT imaging is still controversial in different animal models (Baumann et al., 2015; Dysli et al., 2015; Garcia Garrido et al., 2014; Grieve et al., 2016). Mismatching of or poor correlation between the reflective bands on OCT imaging and histologic sections may result from different sources of error. First, eye positioning during SD-OCT imaging can induce errors. The animal must be positioned with the superior retina located at the upper-most position (Xie et al., 2018 [Fig. 1]). Since the optic nerve head is not located in the center of the porcine fundus and the mean area of the superior retina is about 3-fold larger than the inferior retina (Garca et al., 2005), the superior retina was selected for analysis to reduce error. Second, errors may result from the lack of sectioning the eyeball along the vertical meridian through the optic nerve. This can be minimized by observing the number of

nuclei in the ONL and correcting the orientation of the tissue block to produce the shortest dimension. Similar misalignment may happen during SD-OCT image acquisition. Third, we attempted to acquire both SD-OCT and histological images through the center of the optic nerve and ensure that the histologic sections were obtained at the same location that the OCT B-scan was acquired (Fig. 1, Xie et al., 2018 [Fig. 7]). Finally, tissue processing may induce distortion in the ocular tissues. As per our protocol for tissue handling, fixation in formaldehyde/glutaraldehyde may diminish tissue distortion (Stradleigh and Ishida, 2015).

Minimal tissue shrinkage (about 3%) was observed when comparing total retinal thickness (i.e., vertical direction) by SD-OCT and histology (Fig. 8, Table 1) in the porcine eye. In contrast, significant tissue shrinkage (36 ± 4%) along the transverse (i.e., horizontal) direction of the retina was observed in this study (Xie et al., 2018 [Fig. 7]), similar to a recent report using the same SD-OCT instrument (Yiu et al., 2018). Interestingly, tissue shrinkage in the transverse direction has not been measured in most OCT-histology correlation studies (Gloesmann et al., 2003; Knott et al., 2011; Garcia Garrido et al., 2014). A correlation study of the tree shrew retina showed that axial (i.e., vertical) shrinkage was 28% and lateral (i.e., horizontal) shrinkage was 24.8% after tissue processing with measurements on whole mount micrographs (Abbott et al., 2009). In our study, tissue shrinkage was measured by comparing retinal thickness (i.e., vertical direction) and length (i.e., transverse or horizontal direction) using SD-OCT imaging and histology of corresponding regions in the porcine retina. The apparent discrepancy between the extent of tissue shrinkage in our study compared to the Abbott et al. study might be due to: 1) different methods of histologic tissue processing (e.g., retinal isolation and dissection from the choroid and sclera prior to tissue processing vs. posterior eye cup tissue processing with intact retina-choroid-sclera); 2) the use of different imaging instruments (Zeiss Stratus OCT vs. Heidelberg Spectralis HRA + OCT); 3) differential nonlinear axial shrinkage across retinal sublaminae, as reported in the tree shrew; 4) morphological disparities in the inner and outer retina between the tree shrew and the pig; and 5) interspecies variations in axial length and refractive indices (e.g., the tree shrew eye is about one-third the size of the human or pig eye). Moreover, measurements on the Heidelberg Spectralis HRA + OCT show increased lateral width compared to other commercial SD-OCT instruments (Folgar et al., 2014). Although the size of the pig eye is similar to the human eye, the lateral magnification of the Heidelberg Spectralis HRA + OCT is based on the optics and refractive indices of the human eye rather than the porcine eye. The differences in refractive optics, axial length, retinal tissue composition (e.g., nerve fiber/nuclear/plexiform layer contributions), and optical scattering between the human and porcine eye might contribute to disparities in OCT-histology measurements. In addition, variable lateral/horizontal image stretching or distortion might occur with SD-OCT algorithmic image processing (Chen et al., 2015; Folgar et al., 2014; Garcia Garrido et al., 2015; Podoleanu et al., 2004; Uji et al., 2015, 2017).

Potential limitations of our study include: 1) the use of only one commercially available device to obtain the SD-OCT scans and 2) the use of only one breed of pigs. Nevertheless, our results may be generalizable to the pig as an experimental model for human retinal diseases. In conclusion, the lamellar architecture of the porcine retina imaged with SD-OCT *in vivo* strongly correlated with *ex vivo* histological and ultrastructural examination. Newly described and correlated SD-OCT findings in the porcine retina include: 1) focal, relative hypo-reflectivity in the mid-IPL corresponding to various cell types (most commonly endothelial cells); 2) a hyper-reflective band in the INL corresponding to high concentrations of mitochondria in horizontal cell processes and adjacent bipolar cells; and 3) three outer retinal hyper-reflective bands corresponding to the ELM, EZ, and IZ-RPE complex. These correlative and normative data for *in vivo* morphometric analysis of the porcine retina utilizing SD-OCT may be employed to characterize and evaluate the "histologic" changes in pig models of retinal vascular

and degenerative diseases and responses to novel therapeutic interventions in a large animal model. Additionally, the SD-OCT/TEM correlation in this study may provide an excellent framework for porcine OCT angiography segmentation. The similarities between the porcine and human retina as observed in this study corroborate the utilization of the pig as an excellent large animal model for human retinal diseases.

Declarations of interest

None.

Appendix A. Supplementary data

Supplementary data related to this article can be found at https://doi.org/10.1016/j.exer.2018.08.003.

References

Abbott, C.J., McBrien, N.A., Grunert, U., Pianta, M.J., 2009. Relationship of the optical coherence tomography signal to underlying retinal histology in the tree shrew (Tupaia belangeri). Invest. Ophthalmol. Vis. Sci. 50, 414–423.

Adekunle, A.N., Adkins, A., Wang, W., Kaplan, H.J., de Castro, J.F., Lee, S.J., Huie, P., Palanker, D., McCall, M., Pardue, M.T., 2015. Integration of perforated subretinal prostheses with retinal tissue. Transl. Vis. Technol. 4, 5.

Alamouti, B., Funk, J., 2003. Retinal thickness decreases with age: an OCT study. Br. J. Ophthalmol. 87, 899–901.

Anger, E.M., Unterhuber, A., Hermann, B., Sattmann, H., Schubert, C., Morgan, J.E., Cowey, A., Ahnelt, P.K., Drexler, W., 2004. Ultrahigh resolution optical coherence tomography of the monkey fovea. Identification of retinal sublayers by correlation with semithin histology sections. Exp. Eye Res. 78, 1117–1125.

Asami, T., Terasaki, H., Ito, Y., Sugita, T., Kaneko, H., Nishiyama, J., Namiki, H., Kobayashi, M., Nishizawa, N., 2016. Development of a fiber-optic optical coherence tomography probe for intraocular use. Invest. Ophthalmol. Vis. Sci. 57, 568–574.

Atzpodien, E.A., Jacobsen, B., Funk, J., Altmann, B., Silva Munoz, M.A., Singer, T., Gyger, C., Hasler, P., Maloca, P., 2016. Advanced clinical imaging and tissue-based biomarkers of the eye for toxicology studies in minipigs. Toxicol. Pathol. 44, 398–413.

Avery, R.A., Cnaan, A., Schuman, J.S., Trimboli-Heidler, C., Chen, C.L., Packer, R.J., Ishikawa, H., 2015. Longitudinal change of circumpapillary retinal nerve fiber layer thickness in children with optic pathway gliomas. Am. J. Ophthalmol. 160, 944–952.

Baumann, B., Schirmer, J., Rauscher, S., Fialova, S., Glosmann, M., Augustin, M., Pircher, M., Groger, M., Hitzenberger, C.K., 2015. Melanin pigmentation in rat eyes: in vivo imaging by polarization-sensitive optical coherence tomography and comparison to histology. Invest. Ophthalmol. Vis. Sci. 56, 7462–7472.

Beauchemin, M.L., 1974. The fine structure of the pig's retina. Graefes Clin. Exp. Ophthalmol. 190, 27–45.

Berger, A., Cavallero, S., Dominguez, E., Barbe, P., Simonutti, M., Sahel, J.A., Sennlaub, F., Raoul, W., Paques, M., Bemelmans, A.P., 2014. Spectral-domain optical coherence tomography of the rodent eye: highlighting layers of the outer retina using signal averaging and comparison with histology. PLoS One 9, e96494.

Bloodworth Jr., J.M., Gutgesell Jr., H.P., Engerman, R.L., 1965. Retinal vasculature of the pig. Light and electron microscope studies. Exp. Eye Res. 4, 174–178.

Brant Fernandes, R.A., Koss, M.J., Falabella, P., Stefanini, F.R., Maia, M., Diniz, B., Ribeiro, R., Hu, Y., Hinton, D., Clegg, D.O., Chader, G., Humayun, M.S., 2016. An innovative surgical technique for subretinal transplantation of human embryonic stem cell-derived retinal pigmented epithelium in Yucatan mini pigs: preliminary results. Ophthalmic Surg. Laser. Imag. Retina 47, 342–351.

Carpenter, C.L., Kim, A.Y., Kashani, A.H., 2018. Normative retinal thicknesses in common animal models of eye disease using spectral domain optical coherence tomography. Adv. Exp. Med. Biol. 1074, 157–166.

Chen, Q., de Sisternes, L., Leng, T., Rubin, D.L., 2015. Application of improved homogeneity similarity-based denoising in optical coherence tomography retinal images. J. Digit. Imag. 28, 346–361.

Cuenca, N., Ortuno-Lizaran, I., Pinilla, I., 2018. Cellular characterization of OCT and outer retinal bands using specific immunohistochemistry markers and clinical implications. Ophthalmology 125, 407–422.

Curcio, C.A., Sloan, K.R., Kalina, R.E., Hendrickson, A.E., 1990. Human photoreceptor topography. J. Comp. Neurol. 292, 497–523.

De Schaepdrijver, L., Lauwers, H., Simoens, P., de Geest, J.P., 1990. Development of the retina in the porcine fetus. A light microscopic study. Anat. Histol. Embryol. 19, 222–235.

Dysli, C., Enzmann, V., Sznitman, R., Zinkernagel, M.S., 2015. Quantitative analysis of mouse retinal layers using automated segmentation of spectral domain optical coherence tomography images. Transl. Vis. Sci. Technol. 4, 9.

Ehlers, J.P., Srivastava, S.K., Feiler, D., Noonan, A.I., Rollins, A.M., Tao, Y.K., 2014. Integrative advances for OCT-guided ophthalmic surgery and intraoperative OCT: microscope integration, surgical instrumentation, and heads-up display surgeon feedback. PLoS One 9 e105224.

Fatehee, N., Yu, P.K., Morgan, W.H., Cringle, S.J., Yu, D.Y., 2011. Correlating morphometric parameters of the porcine optic nerve head in spectral domain optical coherence tomography with histological sections. Br. J. Ophthalmol. 95, 585–589.

Folgar, F.A., Yuan, E.L., Farsiu, S., Toth, C.A., 2014. Lateral and axial measurement differences between spectral-domain optical coherence tomography systems. J. Biomed. Optic. 19, 16014.

Fouquet, S., Vacca, O., Sennlaub, F., Paques, M., 2017. The 3D retinal capillary circulation in pigs reveals a predominant serial organization. Invest. Ophthalmol. Vis. Sci. 58, 5754–5763.

Fujimoto, J., Swanson, E., 2016. The development, commercialization, and impact of optical coherence tomography. Invest. Ophthalmol. Vis. Sci. 57, OCT1–OCT13.

Garca, M., Ruiz-Ederra, J., Hernandez-Barbachano, H., Vecino, E., 2005. Topography of pig retinal ganglion cells. J. Comp. Neurol. 486, 361–372.

Garcia Garrido, M., Beck, S.C., Muhlfriedel, R., Julien, S., Schraermeyer, U., Seeliger, M.W., 2014. Towards a quantitative OCT image analysis. PLoS One 9 e100080.

Garcia Garrido, M., Muhlfriedel, R.L., Beck, S.C., Wallrapp, C., Seeliger, M.W., 2015. Scale adjustments to facilitate two-dimensional measurements in OCT images. PLoS One 10 e0131154.

Ghosh, F., Arner, K., 2010. Cell type differentiation dynamics in the developing porcine retina. Dev. Neurosci. 32, 47–58.

Gloesmann, M., Hermann, B., Schubert, C., Sattmann, H., Ahnelt, P.K., Drexler, W., 2003. Histologic correlation of pig retina radial stratification with ultrahigh-resolution optical coherence tomography. Invest. Ophthalmol. Vis. Sci. 44, 1696–1703.

Grieve, K., Paques, M., Dubois, A., Sahel, J., Boccara, C., Le Gargasson, J.F., 2004. Ocular tissue imaging using ultrahigh-resolution, full-field optical coherence tomography. Invest. Ophthalmol. Vis. Sci. 45, 4126–4131.

Grieve, K., Thouvenin, O., Sengupta, A., Borderie, V.M., Paques, M., 2016. Appearance of the retina with full-field optical coherence tomography. Invest. Ophthalmol. Vis. Sci. 57, OCT96–OCT104.

Grover, S., Murthy, R.K., Brar, V.S., Chalam, K.V., 2010. Comparison of retinal thickness in normal eyes using Stratus and Spectralis optical coherence tomography. Invest. Ophthalmol. Vis. Sci. 51, 2644–2647.

Hahn, P., Migacz, J., O'Connell, R., Izatt, J.A., Toth, C.A., 2013. Unprocessed real-time imaging of vitreoretinal surgical maneuvers using a microscope-integrated spectral-domain optical coherence tomography system. Graefes Arch. Clin. Exp. Ophthalmol. 251, 213–220.

Hein, T.W., Potts, L.B., Xu, W., Yuen, J.Z., Kuo, L., 2012. Temporal development of retinal arteriolar endothelial dysfunction in porcine type 1 diabetes. Invest. Ophthalmol. Vis. Sci. 53, 7943–7949.

Hein, T.W., Rosa Jr., R.H., Ren, Y., Xu, W., Kuo, L., 2015. VEGF receptor-2-linked PI3K/calpain/SIRT1 activation mediates retinal arteriolar dilations to VEGF and shear stress. Invest. Ophthalmol. Vis. Sci. 56, 5381–5389.

Hein, T.W., Rosa Jr., R.H., Yuan, Z., Roberts, E., Kuo, L., 2010. Divergent roles of nitric oxide and rho kinase in vasomotor regulation of human retinal arterioles. Invest. Ophthalmol. Vis. Sci. 51, 1583–1590.

Hein, T.W., Xu, W., Xu, X., Kuo, L., 2016. Acute and chronic hyperglycemia elicit JIP1/JNK-mediated endothelial vasodilator dysfunction of retinal arterioles. Invest. Ophthalmol. Vis. Sci. 57, 4333–4340.

Hendrickson, A., Hicks, D., 2002. Distribution and density of medium- and short-wave-length selective cones in the domestic pig retina. Exp. Eye Res. 74, 435–444.

Hoang, Q.V., Linsenmeier, R.A., Chung, C.K., Curcio, C.A., 2002. Photoreceptor inner segments in monkey and human retina: mitochondrial density, optics, and regional variation. Vis. Neurosci. 19, 395–407.

Hogan, M.J., Alvarado, J.A., Weddell, J.E., 1971. Histology of the Human Eye: an Atlas and Textbook. W.B. Saunders, Philadelphia.

Huang, D., Swanson, E.A., Lin, C.P., Schuman, J.S., Stinson, W.G., Chang, W., Hee, M.R., Flotte, T., Gregory, K., Puliafito, C.A., et al., 1991. Optical coherence tomography. Science 254, 1178–1181.

Johansson, U.E., Eftekhari, S., Warfvinge, K., 2010. A battery of cell- and structure-specific markers for the adult porcine retina. J. Histochem. Cytochem. 58, 377–389.

Jonnal, R.S., Kocaoglu, O.P., Zawadzki, R.J., Lee, S.H., Werner, J.S., Miller, D.T., 2014. The cellular origins of the outer retinal bands in optical coherence tomography images. Invest. Ophthalmol. Vis. Sci. 55, 7904–7918.

Kaczurowski, M.I., 1962. The pigment epithelium of the human eye. Am. J. Ophthalmol. 53, 79–92.

Knott, E.J., Sheets, K.G., Zhou, Y., Gordon, W.C., Bazan, N.G., 2011. Spatial correlation of mouse photoreceptor-RPE thickness between SD-OCT and histology. Exp. Eye Res. 92, 155–160.

Koss, M.J., Falabella, P., Stefanini, F.R., Pfister, M., Thomas, B.B., Kashani, A.H., Brant, R., Zhu, D., Clegg, D.O., Hinton, D.R., Humayun, M.S., 2016. Subretinal implantation of a monolayer of human embryonic stem cell-derived retinal pigment epithelium: a feasibility and safety study in Yucatan minipigs. Graefes Arch. Clin. Exp. Ophthalmol. 254, 1553–1565.

Li, Z., Shen, J.H., Kozub, J.A., Prasad, R., Lu, P., Joos, K.M., 2014. Miniature forward-imaging B-scan optical coherence tomography probe to guide real-time laser ablation. Laser Surg. Med. 46, 193–202.

Lim, R.R., Grant, D.G., Olver, T.D., Padilla, J., Czajkowski, A.M., Schnurbusch, T.R., Mohan, R.R., Hainsworth, D.P., Walters, E.M., Chaurasia, S.S., 2018. Young ossabaw pigs fed a western diet exhibit early signs of diabetic retinopathy. Invest. Ophthalmol.

Vis. Sci. 59, 2325–2338.

Litts, K.M., Messinger, J.D., Dellatorre, K., Yannuzzi, L.A., Freund, K.B., Curcio, C.A., 2015a. Clinicopathological correlation of outer retinal tubulation in age-related macular degeneration. JAMA Ophthalmol. 133, 609–612.

Litts, K.M., Messinger, J.D., Freund, K.B., Zhang, Y., Curcio, C.A., 2015b. Inner segment remodeling and mitochondrial translocation in cone photoreceptors in age-related macular degeneration with outer retinal tubulation. Invest. Ophthalmol. Vis. Sci. 56, 2243–2253.

Litts, K.M., Zhang, Y., Freund, K.B., Curcio, C.A., 2018. Optical coherence tomography and histology of age-related macular degeneration support mitochondria as reflectivity sources. Retina 38, 445–461.

Lu, R.W., Curcio, C.A., Zhang, Y., Zhang, Q.X., Pittler, S.J., Deretic, D., Yao, X.C., 2012. Investigation of the hyper-reflective inner/outer segment band in optical coherence tomography of living frog retina. J. Biomed. Optic. 17, 060504.

McLellan, G.J., Rasmussen, C.A., 2012. Optical coherence tomography for the evaluation of retinal and optic nerve morphology in animal subjects: practical considerations. Vet. Ophthalmol. 15 (Suppl. 2), 13–28.

Mones, J., Leiva, M., Pena, T., Martinez, G., Biarnes, M., Garcia, M., Serrano, A., Fernandez, E., 2016. A swine model of selective geographic atrophy of outer retinal layers mimicking atrophic AMD: a phase I escalating dose of subretinal sodium iodate. Invest. Ophthalmol. Vis. Sci. 57, 3974–3983.

Podoleanu, A., Charalambous, I., Plesea, L., Dogariu, A., Rosen, R., 2004. Correction of distortions in optical coherence tomography imaging of the eye. Phys. Med. Biol. 49, 1277–1294.

Ribeiro, L., Bandello, F., Tejerina, A.N., Vujosevic, S., Varano, M., Egan, C., Sivaprasad, S., Menon, G., Massin, P., Verbraak, F.D., Lund-Andersen, H., Martinez, J.P., Jurgens, I., Smets, E., Coriat, C., Wiedemann, P., Agoas, V., Querques, G., Holz, F.G., Nunes, S., Neves, C., Cunha-Vaz, J., 2015. Characterization of retinal disease progression in a 1-year longitudinal study of eyes with mild nonproliferative retinopathy in diabetes type 2. Invest. Ophthalmol. Vis. Sci. 56, 5698–5705.

Rootman, J., 1971. Vascular system of the optic nerve head and retina in the pig. Br. J. Ophthalmol. 55, 808–819.

Rosa Jr., R.H., Glaser, B.M., de la Cruz, Z., Green, W.R., 1996. Clinicopathologic correlation of an untreated macular hole and a macular hole treated by vitrectomy, transforming growth factor-beta 2, and gas tamponade. Am. J. Ophthalmol. 122, 853–863.

Ross, D.H., Clark, M.E., Godara, P., Huisingh, C., McGwin, G., Owsley, C., Litts, K.M., Spaide, R.F., Sloan, K.R., Curcio, C.A., 2015. RefMoB, a reflectivity feature model-based automated method for measuring four outer retinal hyperreflective bands in optical coherence tomography. Invest. Ophthalmol. Vis. Sci. 56, 4166–4176.

Schaal, K.B., Freund, K.B., Litts, K.M., Zhang, Y., Messinger, J.D., Curcio, C.A., 2015. Outer retinal tubulation in advanced age-related macular degeneration: optical coherence tomographic findings correspond to histology. Retina 35, 1339–1350.

Scott, P.A., Fernandez de Castro, J.P., Kaplan, H.J., McCall, M.A., 2014. A Pro23His mutation alters prenatal rod photoreceptor morphology in a transgenic swine model of retinitis pigmentosa. Invest. Ophthalmol. Vis. Sci. 55, 2452–2459.

Scott, P.A., Kaplan, H.J., Sandell, J.H., 2011. Anatomical evidence of photoreceptor degeneration induced by iodoacetic acid in the porcine eye. Exp. Eye Res. 93, 513–527.

Smiddy, W.E., Maguire, A.M., Green, W.R., Michels, R.G., de la Cruz, Z., Enger, C., Jaeger, M., Rice, T.A., 1989. Idiopathic epiretinal membranes. Ultrastructural characteristics and clinicopathologic correlation. Ophthalmology 96, 811–820.

Sorensen, N.F., Ejstrup, R., Svahn, T.F., Sander, B., Kiilgaard, J., la Cour, M., 2012. The effect of subretinal viscoelastics on the porcine retinal function. Graefes Arch. Clin. Exp. Ophthalmol. 250, 79–86.

Spaide, R.F., 2012. Questioning optical coherence tomography. Ophthalmology 119, 2203–2204.

Spaide, R.F., Curcio, C.A., 2011. Anatomical correlates to the bands seen in the outer retina by optical coherence tomography: literature review and model. Retina 31, 1609–1619.

Staurenghi, G., Sadda, S., Chakravarthy, U., Spaide, R.F., 2014. Proposed lexicon for anatomic landmarks in normal posterior segment spectral-domain optical coherence tomography: the IN*OCT consensus. Ophthalmology 121, 1572–1578.

Stradleigh, T.W., Ishida, A.T., 2015. Fixation strategies for retinal immunohistochemistry. Prog. Retin. Eye Res. 48, 181–202.

Tran, J., Craven, C., Wabner, K., Schmit, J., Matter, B., Kompella, U., Grossniklaus, H.E., Olsen, T.W., 2017. A pharmacodynamic analysis of choroidal neovascularization in a porcine model using three targeted drugs. Invest. Ophthalmol. Vis. Sci. 58, 3732–3740.

Ts'o, M.O., Friedman, E., 1967. The retinal pigment epithelium. I. Comparative histology. Arch. Ophthalmol. 78, 641–649.

Ts'o, M.O., Friedman, E., 1968. The retinal pigment epithelium. 3. Growth and development. Arch. Ophthalmol. 80, 214–216.

Tychinsky, V., 2009. The metabolic component of cellular refractivity and its importance for optical cytometry. J. Biophot. 2, 494–504.

Uji, A., Abdelfattah, N.S., Boyer, D.S., Balasubramanian, S., Lei, J., Sadda, S.R., 2017. Variability of retinal thickness measurements in tilted or stretched optical coherence tomography images. Transl. Vis. Sci. Technol. 6, 1.

Uji, A., Murakami, T., Muraoka, Y., Hosoda, Y., Yoshitake, S., Dodo, Y., Arichika, S., Yoshimura, N., 2015. Potential measurement errors due to image enlargement in optical coherence tomography imaging. PLoS One 10 e0128512.

Wang, W., Zhou, L., Lee, S.J., Liu, Y., Fernandez de Castro, J., Emery, D., Vukmanic, E., Kaplan, H.J., Dean, D.C., 2014. Swine cone and rod precursors arise sequentially and display sequential and transient integration and differentiation potential following transplantation. Invest. Ophthalmol. Vis. Sci. 55, 301–309.

Wilson, J.D., Cottrell, W.J., Foster, T.H., 2007. Index-of-refraction-dependent subcellular light scattering observed with organelle-specific dyes. J. Biomed. Optic. 12, 014010.

Xie, W., Zhao, M., Tsai, S., Burkes, W.L., Potts, L.B., Xu, W., Payne, H.R., Hein, T.W., Kuo, L., Rosa Jr., R.H., 2018. Electron microscopy and spectral domain optical coherence tomography of the porcine retina. Exp. Eye Res in this issue.

Yang, Z., Du, S., 1999. Histological measurement of human retinal thickness. J. Tongji Med. Univ. 19, 246–248.

Yiu, G., Wang, Z., Munevar, C., Tieu, E., Shibata, B., Wong, B., Cunefare, D., Farsiu, S., Roberts, J., Thomasy, S.M., 2018. Comparison of chorioretinal layers in rhesus macaques using spectral-domain optical coherence tomography and high-resolution histological sections. Exp. Eye Res. 168, 69–76.